

Coherent Two-State Oscillations in False Vacuum Decay Regimes

Peiyun Ge,^{1,*} Xiao Wang,^{2,1,†} Yu-Xin Chao,¹ Rong Lv,¹ and Li You^{1,2,3,4}

¹State Key Laboratory of Low Dimensional Quantum Physics,

Department of Physics, Tsinghua University, Beijing 100084, China

²Beijing Academy of Quantum Information Sciences, Beijing 100193, China

³Frontier Science Center for Quantum Information, Beijing 100084, China

⁴Hefei National Laboratory, Hefei, Anhui 230088, China

(Dated: September 5, 2025)

Coherent two-state oscillations are observed in numerical simulations of one-dimensional transverse- and longitudinal-field Ising model within the false vacuum decay regimes. Starting from the false vacuum state with all spins up, in moderate-sized systems with a small transverse field, we find conventional decay dynamics at resonance conditions $h \approx 2J/n$ can change into coherent oscillations between the false vacuum and a symmetric resonant state, manifested by a sub-leading eigenstate overlap approaching 0.5 and periodic vanishing of the Loschmidt echo. Notably, the oscillation frequency shows a superradiant-like \sqrt{L} enhancement compared to the earlier Schrieffer-Wolff predictions. In larger systems, we find these oscillations persist for $n \gtrsim L/2$ (enabled by a bubble size blockade effect) or when long-range interactions lift multi-bubble degeneracies, revealing a robust many-body coherence mechanism transcending perturbative treatments and finite-size limitations.

Introduction. Short-range interactions underlie both the formation of domain wall structures [1] and the dynamics of false vacuum decay [2–4]. The latter is a quintessential quantum field theoretic process in which a metastable state decays via nucleation of true vacuum bubbles. This mechanism has far-reaching implications in cosmology [5–7], particle physics [8, 9], and non-equilibrium dynamics [10–14]. While challenging to study in high-energy experiments, this phenomenon has become tractable in NISQ state quantum simulators across a variety of platforms [15–18].

The transverse-longitudinal-field Ising model (TLFIM) provides a paradigmatic platform for studying false vacuum decay. Following Ref. [19], we define the false vacuum state $|\Omega\rangle$ as the ferromagnetic ground state of TLFIM at vanishingly small longitudinal field h . For weak transverse field g , the false vacuum is well approximated by the ferromagnetic all-spin-up state $|\Omega\rangle \approx |\uparrow, \uparrow, \dots, \uparrow\rangle$. Prior studies [16, 20–23] revealed that false vacuum decay proceeds resonantly in the TLFIM when the energetic cost of nucleating a bubble of flipped spins vanishes. Specifically, creating a bubble of size n requires forming two domain walls, which costs the Ising energy $4J$, while simultaneously flipping the n spins inside the bubble gains a Zeeman energy $2nh$ from the longitudinal field h . When the ratio of $2J/h$ approaches an integer n , often referred to as the resonant bubble size (RBS) order, resonant tunnelling is triggered. The condition $2J/h = n$ not only enables resonant coupling between the false vacuum $|\Omega\rangle$ and single-bubble states, it also facilitates sequential resonant tunnelling between single-bubble and *multi-bubble states* [18], i.e., states containing more than one resonant-size bubble. Such sequential tunnelling leads to an exponential decay of the Loschmidt echo [24–26] (i.e., the return probability) of the initial false vacuum state, $P_{\text{ret}}(t) \propto e^{-\Gamma t}$. This decay behaviour

is captured by both the Langer’s droplet expansion (after the 1D–2D quantum–classical mapping) [22, 27, 28] and the Callan–Coleman multi-bounce formalism [3, 4, 29] via Poisson resummation, as well as by more recent Gaussian ansatz approaches [30, 31]. It is understood that in the thermodynamic limit, resonance with multi-bubble states triggers a coherent many-body cascade that drives the incoherent decay of the false vacuum.

Many-body physics arising from short-range interactions is qualitatively modified by long-range interactions. The coexistence of short- and long-range interactions in cold atom platforms such as optical lattices can lead to exotic equilibrium phases [32]. In the topical area of non-equilibrium studies, it has been theoretically proposed that interactions of sufficiently long range can stabilize the coherent oscillations of many-body scars [33].

In this Letter, we report a striking deviation from the conventional false vacuum decay picture in the TLFIM: In small systems with weak transverse fields, coherent two-state oscillations between $|\Omega\rangle$ and a symmetric state $|S_n\rangle$ are detected in numerical simulations, manifested by periodic revivals of the return probability and a sub-leading eigenstate overlap $P_{\text{sub}} \sim 0.5$. We find that the effective Rabi frequency of the oscillation displays a superradiance-like \sqrt{L} enhancement, whose mechanism is captured based on constructing a Schrieffer-Wolff transform (SWT) in a symmetric subspace. For larger systems with stronger transverse fields, we find two mechanisms that can sustain the coherent oscillations: (1) the bubble size blockade effect at $n \gtrsim L/2$, which suppresses multi-bubble states via spatial constraints, and (2) long-range Ising interactions that lift the degeneracy between single- and multi-bubble manifolds. These findings establish a robust framework for many-body coherence that transcends finite-size and perturbative constraints, facilitating quantum simulation and engineering of recurrences

in metastable dynamics.

Model. The TLFIM of length L with periodic boundary conditions is given by

$$\hat{H} = -J \sum_{i=1}^L \hat{\sigma}_i^z \hat{\sigma}_{i+1}^z - g \sum_{i=1}^L \hat{\sigma}_i^x + h \sum_{i=1}^L \hat{\sigma}_i^z, \quad (1)$$

where $\hat{\sigma}_i^z$ and $\hat{\sigma}_i^x$ are Pauli matrices acting on site i , the periodic boundary condition means $\hat{\sigma}_{L+1}^z \equiv \hat{\sigma}_1^z$, and J denotes the strength of the nearest-neighbor (NN) Ising interaction, g denotes transverse field strength, h denotes longitudinal field strength. Throughout this work we set $J = 1$ as the energy unit and concentrate on the ferromagnetic regime where $g < J$.

We start from the false vacuum state $|\Omega\rangle$, obtained as the ground state of the TLFIM with a tiny longitudinal field $h = -0.01$ via exact diagonalization, and observe the dynamics under Hamiltonian (1) with positive h [34]. First, in Fig. 1(a), we observe the minimum return probability, $\min(P_{\text{ret}}(t))$, where $P_{\text{ret}}(t) \equiv |\langle\Omega|e^{-i\hat{H}t}|\Omega\rangle|^2$, over a time window of 400 (in units of J^{-1}). The results clearly reveal whether the system lies within the false vacuum decay regime around $h = 2J/n$ or not, where n is a positive integer between 1 and the system size: the false vacuum decay will significantly suppress the minimum return probability to a vanishing value. Next, in Fig. 1(b), we present the sub-leading overlap between the initial false vacuum state and an eigenstate of the Hamiltonian (1), defined as

$$P_{\text{sub}} \equiv \text{the second largest } P_l, \quad (2)$$

where $P_l = |\langle\Omega|E_l\rangle|^2$, and $|E_l\rangle$ is the l -th eigenstate of the Hamiltonian (1). This overlap serves to detect persistent oscillations between two dominant eigenstates in the decay regime. In particular, when it approaches 0.5, the system's evolution is governed predominantly by just two eigenstates, yielding a persistent many-body two-state coherent oscillation. The regions of near-perfect two-state coherence in Fig. 1(b) lie inside the false vacuum decay regime of Fig. 1(a). Specifically, we find that coherent oscillations appear only when $n \geq 3$, with oscillation period T scaling exponentially with n , $T \sim 2\pi/g^n$. For example, the red dots in Fig. 1(a) mark the corresponding parameters to high-fidelity two-state oscillations ($P_{\text{sub}} > 0.49$) at a period around $T \approx 600$.

In Fig. 1(c), we fix the transverse field at a large value, $g = 0.8$, and plot P_{sub} versus h for increasing L . For a finite system size L , we find that as the longitudinal field h increases from 0 to a small value, the false vacuum decay behaviour is replaced by an alternation between single-state stationary evolution and two-state oscillations, respectively indicated by $P_{\text{sub}} \sim 0$ and $P_{\text{sub}} \sim 0.5$. For $L = 20$, this alternation occurs about five times before entering the false vacuum decay regime. From the vertical blue strips in Fig. 1(b), we infer that the non-trivial resonant states at $g = 0.8$, corresponding to the

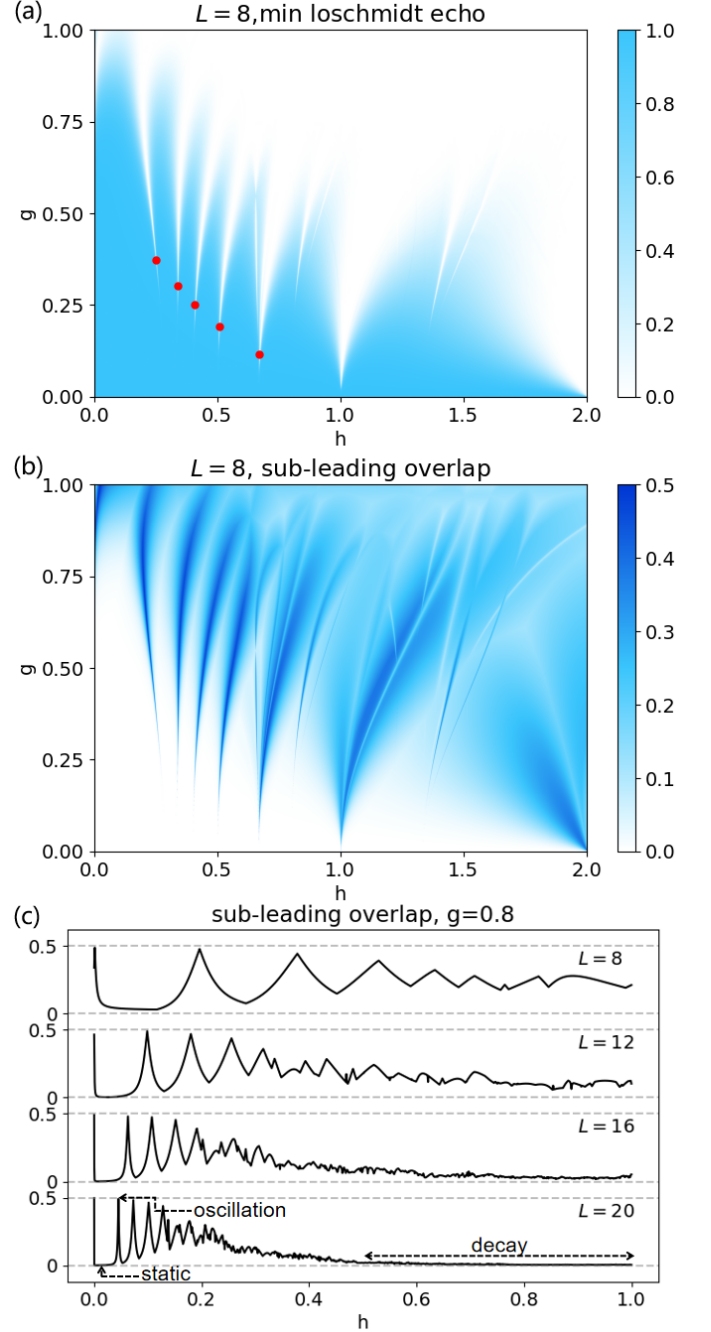


FIG. 1: (a) The minimal return probability $\min(P_{\text{ret}}(t))$ from the false vacuum state $|\Omega\rangle$ for $L = 8$. The Hamiltonian parameters h and g are scanned as x- and y-axis, respectively. (b) The same as (a), but showing the sub-leading overlap P_{sub} between the false vacuum state $|\Omega\rangle$ and the eigenstates of the Hamiltonian (1). The blue regions mark the parameters supporting coherent 2-level dynamics. (c) The sub-leading overlap with $g = 0.8$ for $L = 8, 12, 16$, and 20 .

peaks of P_{sub} in Fig. 1(c), are continuously connected, upon decreasing g , to analytically tractable states. The

latter prove to be the symmetric size- n single-bubble states $|S_n\rangle$, as demonstrated in the following weak- g analysis, where the false vacuum is well approximated by $|\Omega\rangle \approx |\uparrow, \uparrow, \dots, \uparrow\rangle$.

The symmetric resonating state. In Fig. 2, we show the evolution of the initial false vacuum state $|\Omega\rangle$ under the Hamiltonian with $g = 0.11$ and $h = 0.67$. The evolution features a coherent two-state oscillation inside the false vacuum decay regime, with RBS order $n = 2J/h = 3$. The Loschmidt echo, $P_{\text{ret}}(t) \equiv |\langle\Omega|e^{-i\hat{H}t}|\Omega\rangle|^2$, oscillates between 1 and 0 with a certain long period in Fig. 2(a), implicating many-body coherent evolution. As the return probability approaches 0, the local magnetization approaches 0.25 as shown in Fig. 2(b), a coherent resonance between the initial product state and an entangled state emerges, with oscillation period around 680. In Fig. 2(c), the two-site correlations $\langle\hat{Z}_0\hat{Z}_r\rangle$ show that, in this resonant state, ferromagneticity is found at short range, while anti-ferromagneticity permeates at long range. Notably, the correlator $\langle\hat{Z}_0\hat{Z}_3\rangle$ and $\langle\hat{Z}_0\hat{Z}_4\rangle$ are almost the same throughout the dynamics.

The above numerical results suggest that, at a small transverse field $g = 0.11$, the state resonating with the false vacuum state $|\Omega\rangle$ in Fig. 2 is well approximated by

$$|S_3\rangle = \frac{1}{\sqrt{L}} \sum_i \hat{S}_{i-1}^- \hat{S}_i^- \hat{S}_{i+1}^- |\Omega\rangle, \quad (3)$$

where $\hat{S}_i^- \equiv |\downarrow\rangle_i \langle\uparrow|$ flips the spin at site i . The symmetric state $|S_3\rangle$ contains a single bubble with length 3 and remains invariant under site translation $i \rightarrow i+1$ on the L -site periodic ring. Moreover, we find that the coherent two-state evolution can be approximated by the following Bloch-sphere dynamics

$$e^{-i\hat{H}t}|\Omega\rangle \approx e^{-i\nu_g t} \left[\cos\left(\frac{\omega}{2}t\right) |\Omega\rangle - i \sin\left(\frac{\omega}{2}t\right) |S_3\rangle \right], \quad (4)$$

where $\omega = 2\pi/T$ is the observed oscillation frequency, while ν_g is the global phase. As detailed in the Supplemental material (SM) Sec. I, the dynamics in Fig. 2 can be completely explained by Eq. (4). Next, we provide an analytical calculation of the frequency ω .

The enhanced oscillation frequency. At the false vacuum decay resonance $h = 2J/n$ with small g , an effective two-state model is developed based on Schrieffer-Wolff transform (SWT) [35]. Specifically, for $n = 3$ or $h = 2J/3$, the SWT treatment gives [35]

$$H_{\text{eff}} \approx E_0(h) + \begin{bmatrix} 0 & -\frac{81}{64}g^3 \\ -\frac{81}{64}g^3 & 4 - 6h \end{bmatrix}. \quad (5)$$

However, we find this result cannot accurately reproduce the observed oscillatory frequency ω in Eq. (4). Moreover, Ref. [18] provides a complicated projected many-body Hamiltonian given by the leading order SWT [see Eq.(25) in its Supplemental material]. Since the all-up

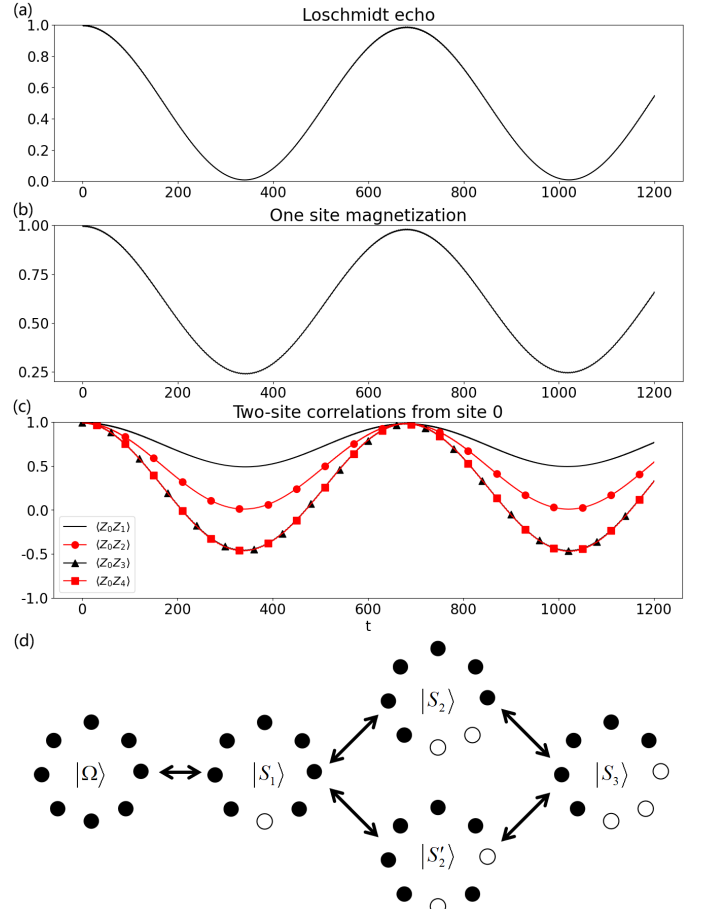


FIG. 2: The evolution starting from the false vacuum state $|\Omega\rangle$ with $L = 8$, $h = 0.67$ and $g = 0.11$. (a) The Loschmidt return probability to the initial state. (b) The one-site magnetization. (c) The ZZ correlator. The values of $\langle Z_0 Z_3 \rangle$ and $\langle Z_0 Z_4 \rangle$ are nearly identical, as explained in the SM. (d) The five translationally invariant states closely support the oscillation.

state is an eigenstate of the corresponding many-body Hamiltonian, Ref. [18] cannot explain the two-state coherent oscillation we have observed within the false vacuum decay regime either.

To improve upon the above SWT result, we work in the subspace spanned by 5 symmetric states (as illustrated in Fig. 2) and conduct SWT to the third order in g . The resulting effective two-state Hamiltonian consequently reads (see SM Sec. II)

$$H_{\text{eff}}^{\text{mod}} \approx E_0(h, g) + \begin{bmatrix} \Delta(h, g, L) & -\kappa(h)\sqrt{L}g^3 \\ -\kappa(h)\sqrt{L}g^3 & 4 - 6h \end{bmatrix}, \quad (6)$$

where Δ represents an $O(g^2)$ shift of self-energy for the false vacuum state $|\Omega\rangle$, and κ is a coefficient which evaluates to $\frac{81}{64}$ when $h = \frac{2}{3}$, namely when $|\Omega\rangle$ resonates with $|S_3\rangle$. The self-energy term was not provided in Ref. [35]. Most importantly, we find the effective Rabi frequency

scales as \sqrt{L} , characteristic of a superradiance-like collective enhancement. A similar \sqrt{L} scaling was experimentally reported in fully Rydberg-blockaded systems [36], wherein only one atom can be excited [37]. This modified effective Hamiltonian (6) gives, in the resonant case, the oscillation period $\frac{\pi}{\kappa\sqrt{L}g^3} \sim 659$, which corroborates well with the numerical simulations.

The bubble size blockade effect. For larger ring length L , the effective two-state coherent oscillation persists at larger RBS orders, namely when $n \gtrsim L/2$. We interpret this behaviour as the bubble size blockade effect, explained as follows. Near the order- n false vacuum decay when $h \approx 2J/n$, a bubble with size n is resonating with the false vacuum, but the states with multiple bubbles are also at resonance, and their participation in the dynamics leads to faster thermalization. However, as n approaches L , the multi-bubble states can no longer exist (due to the restriction set by the ring size L), and thus the dynamics is restricted between the false vacuum and the one-bubble state manifold, hence a coherent two-state oscillation arises. This effect is presented in Fig. 3. In a ring with $L = 12$, we plot the P_{sub} around RBS orders $n = 3 \sim 6$. At larger RBS orders $n = 5, 6$, near-perfect coherence is observed with P_{sub} approaching 0.5, as explained by the bubble size blockade. Around smaller orders $n = 3$ and $n = 4$, the blockade effect vanishes because states with 2 or 3 bubbles can enter into the dynamics. Consequently, as L increases from 8 to 12, the overlap P_{sub} at $n = 3$ still exhibits a blue regime but no longer approaches 0.5.

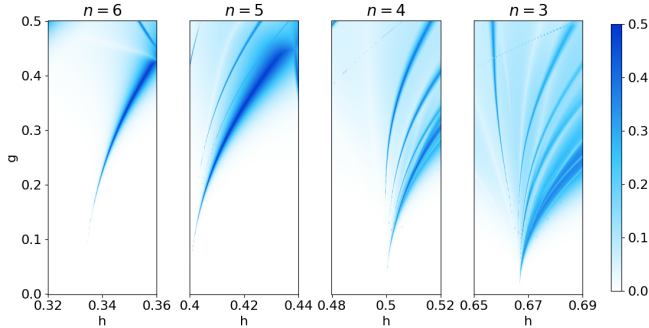


FIG. 3: The sub-leading overlap between the false vacuum state and the eigenstates of the Hamiltonian (1) for $L = 12$.

For even larger L , whenever $n \gtrsim L/2$, we expect the same blockade effect (provided that the transverse field g is not too large to break it), which underlies the alternations of P_{sub} shown in Fig. 1 (c). As n increases at fixed g , the blue regime in the diagram of P_{sub} becomes exponentially narrower, making it increasingly difficult to identify parameters that facilitate the two-state oscillation. Nevertheless, at large g this narrowing problem is mitigated, and Fig. 1 (c) further shows that the bubble

size blockade effect persists even at such large g , where the all-up state no longer approximates the false vacuum. Thus, for a moderate chain size $L = 20$, coherent two-state oscillations can still be observed at $n = 19$ and $g = 0.8$. Moreover, for the blockade-facilitated two-state oscillations in this large- g regime, we find these oscillations are robust against interaction disorder, as shown in the SM Sec. III. This robustness may originate from the non-local nature of domain walls at large g [38], which effectively averages out local fluctuations in the interaction strength.

Lifting the degeneracy of the multi-bubble manifold. For large L , another way enabling the two-state dynamics arises, not necessarily at a large n , but by introducing long-range Ising interactions, with which the interaction between bubbles can no longer be neglected. As a result, the state degeneracy between the single-bubble manifold and the multi-bubble manifold is lifted. Consequently, the multi-bubble states can no longer enter into the oscillatory dynamics between $|\Omega\rangle$ and $|S_n\rangle$, even outside the bubble size blockade effect regime ($n < L/2$). For example, as shown in Fig. 4, for an $L = 12$ ring with r^{-3} long-range Ising interactions (with the Ising term modified into $-J \sum_{i < j} |i - j|^{-3} \hat{\sigma}_i^z \hat{\sigma}_j^z$ [39, 40]), the sub-leading overlap P_{sub} around $n = 3$ can again reach 0.5. A detailed explanation is given in the SM Sec. IV, which shows that the dynamics of two-state oscillation can still be approximated by Eqs. (4) and (6), with the parameters κ and Δ renormalized by the long range part of the interaction.

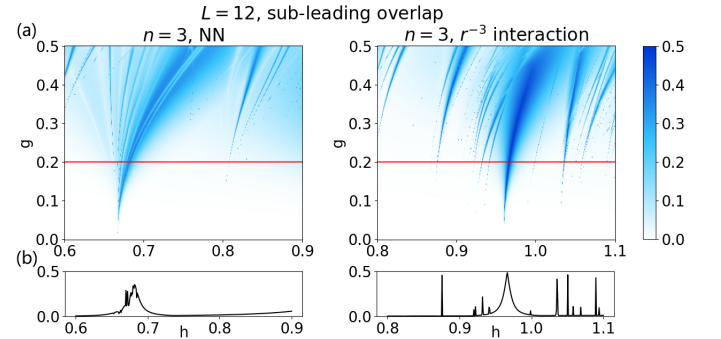


FIG. 4: (a) The sub-leading overlap between the false vacuum state and the eigenstates of \hat{H} . The left panel corresponds to the NN Ising model in Eq. (1). The right panel shows the model with r^{-3} type interactions. (b) Horizontal cut of (a) at $g = 0.2$ for $L = 12$.

For even larger systems, we can use global-range interactions to stabilize coherent two-state oscillations. As shown in SM Sec. V for an $L = 16$ ring, by adding a cavity-mediated spin-squeezing term $-\frac{\beta J}{L} (\sum_{i=1}^L \hat{\sigma}_i^z)^2$ to the Hamiltonian (1), we find that this global-range interaction pushes the forest of multi-bubble resonances outside the single-bubble resonance, thereby enhancing

the coherence of the oscillation between $|\Omega\rangle$ and $|S_3\rangle$.

The coherent orbital. Beyond single-bubble resonant physics of the false vacuum $|\Omega\rangle$, we find that by further quenching the longitudinal field h , the afore-mentioned $|S_n\rangle$ can resonantly couple to multi-bubble states, forming orbital-like structures through consecutive two-state oscillations. Long-range interactions further enrich these coherent orbitals through degeneracy lifting and branch-splitting, suggesting applications in quantum information processing and interferometry (see SM Sec. VI).

Conclusions. In this work we have uncovered a coherent, two-state oscillation phenomenon that arises within the false vacuum decay regime of the TLFIM. By preparing the system in the false vacuum state, we show that for small system sizes and weak transverse field, the familiar resonant decay expected at $h \approx 2J/n$ gives way to sustained Rabi-like oscillations between the false vacuum and a symmetric resonant state. We construct the modified SWT in the symmetric subspace, which reveals a \sqrt{L} superradiance-like enhancement on the effective Rabi frequency, in agreement with numerical observations.

We further show that this coherent behaviour extends beyond small systems, surviving in larger chains whenever the resonant bubble size satisfies $n \gtrsim L/2$ (bubble size blockade) or when long-range interactions lift multi-bubble degeneracies. These results establish a robust many-body coherence mechanism persisting beyond finite size and weak quantum fluctuations. Moreover, with properly engineered inter-domain interactions, a coherent orbital can be created. Our findings therefore open new avenues for exploring controlled coherent dynamics in false vacuum settings and may facilitate near-term quantum simulation of recurrences in many-body physics [41] relevant to meta-stability [42], spectral entropy [43], collective gates of qubit chains [44], and interaction-based nonlinear interferometric readout [45].

Acknowledgments. XW thanks the Gongji Cloud for the support of the computational resources for plotting the phase diagrams, and appreciates helpful discussions with Xin Chen, Laura Batini, and Xinhui Liang.

* These authors contributed equally to this work.

† These authors contributed equally to this work.; xw970921@gmail.com

- [1] A. Bray, Theory of phase-ordering kinetics, *Adv. Phys.* **43**, 357 (1994).
- [2] S. Coleman, Fate of the false vacuum: Semiclassical theory, *Phys. Rev. D* **15**, 2929 (1977).
- [3] C. G. Callan and S. Coleman, Fate of the false vacuum. ii. first quantum corrections, *Phys. Rev. D* **16**, 1762 (1977).
- [4] F. Devoto, S. Devoto, L. Di Luzio, and G. Ridolfi, False vacuum decay: an introductory review, *J. Phys. G: Nucl. Part. Phys.* **49**, 103001 (2022).
- [5] S. Coleman and F. De Luccia, Gravitational effects on and of vacuum decay, *Phys. Rev. D* **21**, 3305 (1980).
- [6] A. H. Guth, Inflationary universe: A possible solution to the horizon and flatness problems, *Phys. Rev. D* **23**, 347 (1981).
- [7] A. Vilenkin, Quantum creation of universes, *Phys. Rev. D* **30**, 509 (1984).
- [8] G. Isidori, G. Ridolfi, and A. Strumia, On the metastability of the standard model vacuum, *Nucl. Phys. B* **609**, 387 (2001).
- [9] D. Buttazzo, G. Degrassi, P. P. Giardino, G. F. Giudice, F. Sala, A. Salvio, and A. Strumia, Investigating the near-criticality of the higgs boson, *J. High Energy Phys.* **2013** (12), 89.
- [10] J. S. Langer, Theory of nucleation rates, *Phys. Rev. Lett.* **21**, 973 (1968).
- [11] O. Fialko, B. Opanchuk, A. I. Sidorov, P. D. Drummond, and J. Brand, Fate of the false vacuum: Towards realization with ultra-cold atoms, *Europhys. Lett.* **110**, 56001 (2015).
- [12] J. Braden, M. C. Johnson, H. V. Peiris, A. Pontzen, and S. Weinfurtner, Nonlinear dynamics of the cold atom analog false vacuum, *J. High Energy Phys.* **2019** (10), 174.
- [13] T. P. Billam, R. Gregory, F. Michel, and I. G. Moss, Simulating seeded vacuum decay in a cold atom system, *Phys. Rev. D* **100**, 065016 (2019).
- [14] L. Batini, A. Chatrchyan, and J. Berges, Real-time dynamics of false vacuum decay, *Phys. Rev. D* **109**, 023502 (2024).
- [15] Z.-H. Zhu, Y. Liu, G. Lagnese, F. M. Surace, W.-Y. Zhang, M.-G. He, J. C. Halimeh, M. Dalmonte, S. C. Morampudi, F. Wilczek, Z.-S. Yuan, and J.-W. Pan, Probing false vacuum decay on a cold-atom gauge-theory quantum simulator (2024), [arXiv:2411.12565](https://arxiv.org/abs/2411.12565) [[cond-mat.quant-gas](https://arxiv.org/abs/2411.12565)].
- [16] A. Zenesini, A. Berti, R. Cominotti, C. Rogora, I. G. Moss, T. P. Billam, I. Carusotto, G. Lamporesi, A. Recati, and G. Ferrari, False vacuum decay via bubble formation in ferromagnetic superfluids, *Nat. Phys.* **20**, 558 (2024).
- [17] D. Luo, F. M. Surace, A. De, A. Leroose, E. R. Bennewitz, B. Ware, A. Schuckert, Z. Davoudi, A. V. Gorshkov, O. Katz, and C. Monroe, Quantum simulation of bubble nucleation across a quantum phase transition (2025), [arXiv:2505.09607](https://arxiv.org/abs/2505.09607) [[quant-ph](https://arxiv.org/abs/2505.09607)].
- [18] J. Vodeb, J.-Y. Desaulles, A. Hallam, A. Rava, G. Humar, D. Willsch, F. Jin, M. Willsch, K. Michielsen, and Z. Papić, Stirring the false vacuum via interacting quantized bubbles on a 5,564-qubit quantum annealer, *Nat. Phys.* **21**, 386–392 (2025).
- [19] G. Lagnese, F. M. Surace, S. Morampudi, and F. Wilczek, Detecting a long-lived false vacuum with quantum quenches, *Phys. Rev. Lett.* **133** (2024).
- [20] G. Lagnese, F. M. Surace, M. Kormos, and P. Calabrese, False vacuum decay in quantum spin chains, *Phys. Rev. B* **104**, L201106 (2021).
- [21] S. Darbha, M. Kornjača, F. Liu, J. Balewski, M. R. Hirsbrunner, P. L. S. Lopes, S.-T. Wang, R. Van Beeumen, D. Camps, and K. Klymko, False vacuum decay and nucleation dynamics in neutral atom systems, *Phys. Rev. B* **110**, 155103 (2024).
- [22] S. B. Rutkevich, Decay of the metastable phase in $d = 1$ and $d = 2$ ising models, *Phys. Rev. B* **60**, 14525 (1999).
- [23] M. Lencsés, G. Mussardo, and G. Takács, Variations on vacuum decay: The scaling ising and tricritical ising field theories, *Phys. Rev. D* **106**, 105003 (2022).

- [24] H. T. Quan, Z. Song, X. F. Liu, P. Zanardi, and C. P. Sun, Decay of loschmidt echo enhanced by quantum criticality, *Phys. Rev. Lett.* **96**, 140604 (2006).
- [25] S. Sharma, A. Russomanno, G. E. Santoro, and A. Dutta, Loschmidt echo and dynamical fidelity in periodically driven quantum systems, *Europhys. Lett.* **106**, 67003 (2014).
- [26] J. J. Mendoza-Arenas, Dynamical quantum phase transitions in the one-dimensional extended fermi-hubbard model, *J. Stat. Mech: Theory Exp.* **2022**, 043101 (2022).
- [27] J. Langer, Statistical theory of the decay of metastable states, *Ann. Phys.* **54**, 258 (1969).
- [28] H. L. Richards, M. A. Novotny, and P. A. Rikvold, Analytical and computational study of magnetization switching in kinetic ising systems with demagnetizing fields, *Phys. Rev. B* **54**, 4113 (1996).
- [29] M. Carosi and B. Garbrecht, False vacuum decay beyond the quadratic approximation: Summation of non-local self-energies, *Phys. Rev. D* **111** (2025).
- [30] C. Johansen, A. Recati, I. Carusotto, and A. Biella, Many-body theory of false vacuum decay in quantum spin chains (2025), [arXiv:2508.13780 \[cond-mat.stat-mech\]](#).
- [31] D. Maertens, J. Haegeman, and K. V. Acoleyen, Real-time bubble nucleation and growth for false vacuum decay on the lattice (2025), [arXiv:2508.13645 \[cond-mat.stat-mech\]](#).
- [32] R. Landig, L. Hruby, N. Dogra, M. Landini, R. Mottl, T. Donner, and T. Esslinger, Quantum phases from competing short- and long-range interactions in an optical lattice, *Nature* **532**, 476.
- [33] A. Lerose, T. Parolini, R. Fazio, D. A. Abanin, and S. Pappalardi, Theory of robust quantum many-body scars in long-range interacting systems, *Phys. Rev. X* **15**, 011020 (2025).
- [34] Although the definitions of the false vacuum in Refs. [20] and [19] differ slightly, they yield essentially the same results in our work.
- [35] A. Sinha, T. Chanda, and J. Dziarmaga, Nonadiabatic dynamics across a first-order quantum phase transition: Quantized bubble nucleation, *Phys. Rev. B* **103**, L220302 (2021).
- [36] H. Labuhn, D. Barredo, S. Ravets, S. de Léséleuc, T. Macrì, T. Lahaye, and A. Browaeys, Tunable two-dimensional arrays of single Rydberg atoms for realizing quantum Ising models, *Nature* **534**, 667 (2016).
- [37] Apart from the fully blockade case, Ref. [36] also explored the nearest neighbor blockade region in their Fig. 3b, corresponding to the $n = 1$ RBS order. However, in Fig. 1(b), we see that $n = 1$ cannot sustain two-state coherence.
- [38] A numerical study of this non-local behaviour of domain walls is given in Ref. [46].
- [39] P. Jurcevic, B. P. Lanyon, P. Hauke, C. Hempel, P. Zoller, R. Blatt, and C. F. Roos, Quasiparticle engineering and entanglement propagation in a quantum many-body system, *Nature* **511**, 202 (2014).
- [40] J. Zhang, G. Pagano, P. W. Hess, A. Kyprianidis, P. Becker, H. Kaplan, A. V. Gorshkov, Z.-X. Gong, and C. Monroe, Observation of a many-body dynamical phase transition with a 53-qubit quantum simulator, *Nature* **551**, 601 (2017).
- [41] D. Barredo, H. Labuhn, S. Ravets, T. Lahaye, A. Browaeys, and C. S. Adams, Coherent excitation transfer in a spin chain of three rydberg atoms, *Phys. Rev. Lett.* **114**, 113002 (2015).
- [42] C. Yin, F. M. Surace, and A. Lucas, Theory of metastable states in many-body quantum systems, *Phys. Rev. X* **15**, 011064 (2025).
- [43] X. Wang, X. He, and J. Wu, Many-body quantum geometry in time-dependent quantum systems with emergent quantum field theory instantaneously (2025), [arXiv:2503.18396 \[cond-mat.str-el\]](#).
- [44] A. Cao, W. J. Eckner, T. Lukin Yelin, A. W. Young, S. Jandura, L. Yan, K. Kim, G. Pupillo, J. Ye, N. Darkwah Oppong, et al., Multi-qubit gates and schrödinger cat states in an optical clock, *Nature* **634**, 315 (2024).
- [45] Q. Liu, L.-N. Wu, J.-H. Cao, T.-W. Mao, X.-W. Li, S.-F. Guo, M. K. Tey, and L. You, Nonlinear interferometry beyond classical limit enabled by cyclic dynamics, *Nat. Phys.* **18**, 167 (2022).
- [46] A. Milsted, J. Liu, J. Preskill, and G. Vidal, Collisions of false-vacuum bubble walls in a quantum spin chain, *PRX Quantum* **3**, 020316 (2022).

Supplemental Material

Coherent Two-State Oscillations in False Vacuum Decay Regimes

Peiyun Ge¹, Xiao Wang^{2,1}, Yu-Xin Chao¹, Rong Lv¹, and Li You^{1,2,3,4}

¹*State Key Laboratory of Low Dimensional Quantum Physics,*

Department of Physics, Tsinghua University, Beijing 100084, China

²*Beijing Academy of Quantum Information Sciences, Beijing 100193, China*

³*Frontier Science Center for Quantum Information, Beijing 100084, China*

⁴*Hefei National Laboratory, Hefei, Anhui 230088, China*

In this Supplemental Material, we provide additional derivations and details that supporting the main results of the Letter. In Section I we explain the coherent dynamics observed in Fig. 2 using Eqs. (3) and (4) of the main text. In Section II, we construct the SWT in the symmetric subspace and derive the effective two-state Hamiltonian showing a superradiant-like enhancement of the oscillation frequency. In Section III we demonstrate the robustness of the two-state oscillation against the interaction disorder in the blockade-facilitated large- g regime. In Section IV we show numerically that the coherent two-state oscillation with r^{-3} long-range interactions can still be described by Eq. (4). In Section V we show that in large systems, the coherence of the two-state oscillation can be drastically enhanced by cavity-mediated global-range interactions. In Section VI we analyze the coherent orbital structure arising from the consecutive coherent two-state oscillations starting from the symmetric state $|S_n\rangle$.

I. EXPLANATION OF THE OBSERVED COHERENT DYNAMICS IN FIG. 2

In the regime of $h \sim \frac{2J}{n}$ and small g , the false vacuum state is expected to be resonant with the symmetric single-bubble state with bubble size n , defined as $|S_n\rangle = \frac{1}{\sqrt{L}} \sum_i \hat{S}_i^- \hat{S}_{i+1}^- \dots \hat{S}_{i+n-1}^- |\Omega\rangle$ where $|\Omega\rangle \approx |\uparrow, \uparrow, \dots, \uparrow\rangle$. [For example, see Eq. (3) in the main text for $|S_3\rangle$.] In Fig. 2, when the initial false vacuum state evolves into $|S_n\rangle$, the magnetization approaches $m(L, n) = \frac{L-2n}{L}$ and the two-site correlation $\langle Z_0 Z_r \rangle$ can be expressed as $\langle Z_0 Z_r \rangle = \frac{L-2N(L, n, r)}{L}$, where $N(L, n, r)$ denotes the number of spin pairs with opposite directions separated by distance r ,

$$N(L, n, r) = \begin{cases} 2r, & 1 \leq r < k, \\ 2k, & k \leq r \leq \frac{L}{2}. \end{cases} \quad (7)$$

where $k = \min(n, L-n)$, $1 \leq r \leq L/2$. For example, when $L = 8$ and $n = 3$, one finds $N(r=1) = 2$, $N(r=2) = 4$, $N(r=3) = 6$, $N(r=4) = 6$, so $\langle Z_0 Z_1 \rangle = \frac{1}{2}$, $\langle Z_0 Z_2 \rangle = 0$, $\langle Z_0 Z_3 \rangle = -\frac{1}{2}$, $\langle Z_0 Z_4 \rangle = -\frac{1}{2}$, which are in quantitative agreement with the correlations shown in Fig. 2.

II. THE EFFECTIVE TWO-STATE HAMILTONIAN GIVEN BY SWT

We separate the Hamiltonian (1) into $\hat{H} = \hat{H}_0 + \hat{H}^{(1)}$, where $\hat{H}^{(1)}$ represents the transverse field. Near the $n = 3$ resonance, we restrict \hat{H} to a subspace spanned by 5 symmetric states, $\{|\Omega\rangle = |\uparrow\uparrow\dots\rangle, |S_1\rangle = \frac{1}{\sqrt{L}} \sum_i \hat{S}_i^- |\Omega\rangle, |S_2\rangle = \frac{1}{\sqrt{L}} \sum_i \hat{S}_i^- \hat{S}_{i+1}^- |\Omega\rangle, |S'_2\rangle = \frac{1}{\sqrt{L}} \sum_i \hat{S}_i^- \hat{S}_{i+2}^- |\Omega\rangle, |S_3\rangle = \frac{1}{\sqrt{L}} \sum_i \hat{S}_i^- \hat{S}_{i+1}^- \hat{S}_{i+2}^- |\Omega\rangle\}$ as shown in Fig. 2. In this subspace, the unperturbed term becomes a diagonal matrix,

$$\hat{H}_0 = \begin{pmatrix} -L + Lh & & & & \\ & 4 - L + (L-2)h & & & \\ & & 4 - L + (L-4)h & & \\ & & & 8 - L + (L-4)h & \\ & & & & 4 - L + (L-6)h \end{pmatrix}, \quad (8)$$

and the perturbation term reads

$$\hat{H}^{(1)} = -g \begin{pmatrix} 0 & \sqrt{L} & 0 & 0 & 0 \\ \sqrt{L} & 0 & 2 & 2 & 0 \\ 0 & 2 & 0 & 0 & 2 \\ 0 & 2 & 0 & 0 & 1 \\ 0 & 0 & 2 & 1 & 0 \end{pmatrix}. \quad (9)$$

Near $n = 3$ resonance, a block-diagonal structure emerges from the degeneracy of \hat{H}_0 , where $|\Omega\rangle$ and $|S_3\rangle$ span a degenerate block. In the Schrieffer-Wolff transform,

$$\begin{aligned}\hat{H}' = e^{\hat{S}} \hat{H} e^{-\hat{S}} &= \hat{H}_0 + \hat{H}^{(1)} + [\hat{S}, \hat{H}_0 + \hat{H}^{(1)}] \\ &+ \frac{1}{2!} [\hat{S}, [\hat{S}, \hat{H}_0 + \hat{H}^{(1)}]] \\ &+ \frac{1}{3!} [\hat{S}, [\hat{S}, [\hat{S}, \hat{H}_0 + \hat{H}^{(1)}]]] + \dots,\end{aligned}\quad (10)$$

the anti-Hermitian operator \hat{S} is chosen to eliminate the off-block-diagonal term in the transformed Hamiltonian \hat{H}' . We expand \hat{S} in orders of g , $\hat{S} = \sum_{i=n}^{\infty} \hat{S}^{(i)}$, such that $\hat{S}^{(i)}$ eliminates the $O(g^n)$ off-block-diagonal term in \hat{H}' . By eliminating the off-block-diagonal terms to $O(g)$ and then $O(g^2)$ order, we respectively obtain $\hat{S}^{(1)}$ and $\hat{S}^{(2)}$, i.e.,

$$\hat{S}^{(1)} = -g \begin{pmatrix} 0 & \frac{\sqrt{L}}{2(h-2)} & 0 & 0 & 0 \\ -\frac{\sqrt{L}}{2h-4} & 0 & \frac{1}{h} & \frac{1}{h-2} & 0 \\ 0 & -\frac{1}{h} & 0 & 0 & \frac{1}{h} \\ 0 & -\frac{1}{h-2} & 0 & 0 & \frac{1}{2(h+2)} \\ 0 & 0 & -\frac{1}{h} & -\frac{1}{2h+4} & 0 \end{pmatrix}, \quad (11)$$

$$\hat{S}^{(2)} = g^2 \begin{pmatrix} 0 & 0 & \frac{4\sqrt{L}}{h(16h^2-48h+32)} & 0 & 0 \\ 0 & 0 & 0 & 0 & \frac{2}{h(4h^2-16)} \\ -\frac{4\sqrt{L}}{h(16h^2-48h+32)} & 0 & 0 & \frac{16h^2+48h-32}{h(64h^2-256)} & 0 \\ 0 & 0 & \frac{-16h^2-48h+32}{h(64h^2-256)} & 0 & 0 \\ 0 & -\frac{2}{h(4h^2-16)} & 0 & 0 & 0 \end{pmatrix}. \quad (12)$$

The effective two-state Hamiltonian, correct to $O(g^3)$, is then extracted from the degenerate block, which reads

$$\hat{H}_{eff}^{mod} = \begin{pmatrix} \langle \Omega | \hat{H}' | \Omega \rangle & \langle \Omega | \hat{H}' | S_3 \rangle \\ \langle S_3 | \hat{H}' | \Omega \rangle & \langle S_3 | \hat{H}' | S_3 \rangle \end{pmatrix} = \begin{pmatrix} \frac{Lg^2}{2h-4} + L(h-1) & -\frac{(h(9h-10)-8)g^3\sqrt{L}}{12(h-2)^2h^2(h^2+h-2)} \\ -\frac{(h(9h-10)-8)g^3\sqrt{L}}{12(h-2)^2h^2(h^2+h-2)} & -\frac{g^2(5h+8)}{2h(h+2)} - L + h(L-6) + 4 \end{pmatrix} + O(g^4). \quad (13)$$

In Eq. (13), the $O(g^0)$ term represents the energy detuning in \hat{H}_0 . The $O(g^2)$ diagonal self-energy term comes from the second-order virtual process, akin to the AC Stark shift. The $O(g^3)$ term serves as the Rabi frequency of the effective two-state dynamics, and the \sqrt{L} enhancement comes from the normalization factor of the symmetric state. The main text's Eq. (6) is recovered from Eq. (13) by defining

$$\begin{aligned}\kappa(h) &= \frac{h(9h-10)-8}{12(h-2)^2h^2(h^2+h-2)}, \\ E_0(h, g) &= -\frac{g^2(5h+8)}{2h(h+2)} + L(h-1), \\ \Delta(h, g, L) &= g^2 \left(\frac{L}{2h-4} + \frac{(5h+8)}{2h(h+2)} \right).\end{aligned}\quad (14)$$

III. ROBUSTNESS AGAINST DISORDER INTERACTION AT LARGE g

In real experiments, fluctuations in the spin-spin distance lead to a modified Hamiltonian,

$$\hat{H} = -\sum_{i=1}^L J_i \hat{\sigma}_i^z \hat{\sigma}_{i+1}^z - g \sum_{i=1}^L \hat{\sigma}_i^x + h \sum_{i=1}^L \hat{\sigma}_i^z, \quad (15)$$

where the couplings J_i are modeled as Gaussian variables centered at J with standard deviation σ . For this Hamiltonian, we compute the disorder-averaged dynamics over 100 realizations, which provides experimentally relevant expectation values. As shown in Fig. S1, at the $n = 11$ resonance with a relatively weak transverse field $g = 0.6$, the Loschmidt echo and magnetization are highly sensitive to disorder, such that for deviation $\sigma = 0.02$ the coherent oscillations are substantially suppressed. In contrast, Fig. S2 demonstrates that for a larger transverse field $g = 0.8$, the dynamics at the $n = 11$ resonance remain nearly unchanged until the disorder strength exceeds $\sigma \gtrsim 0.05$.

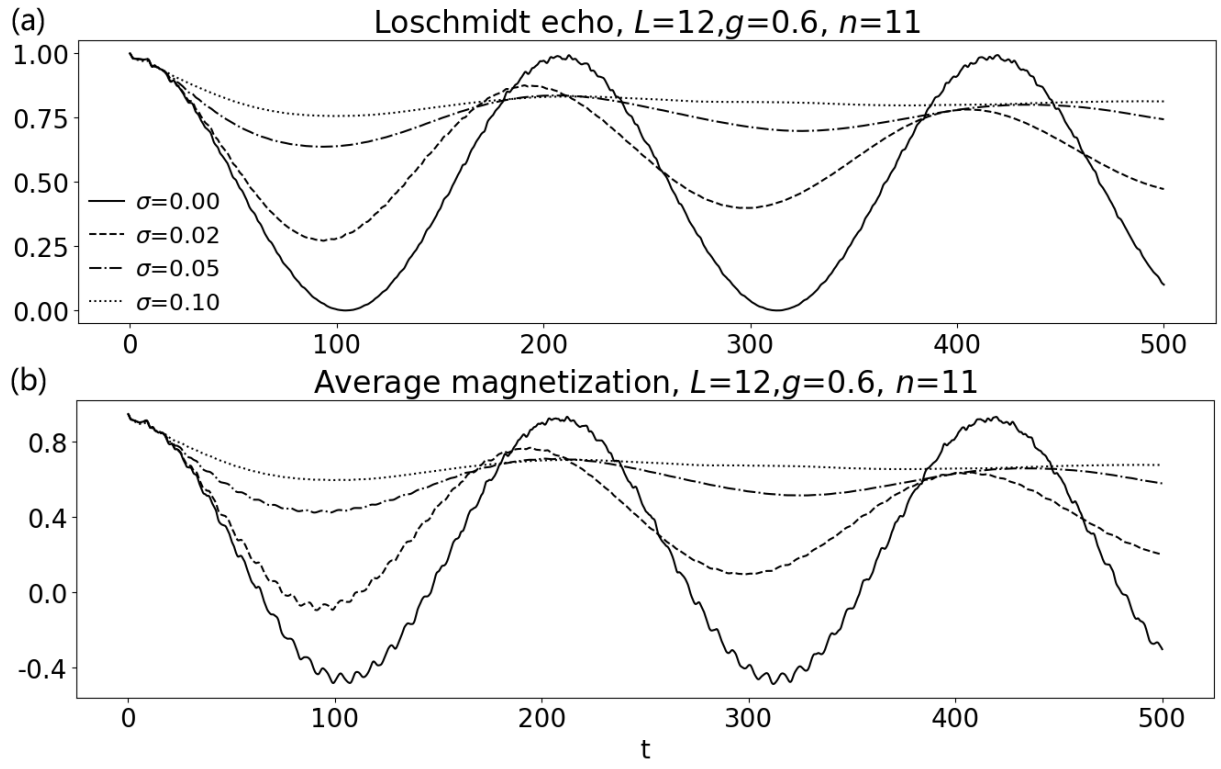


FIG. S1: Dynamics of an $L = 12$ ring at $g = 0.6$, evaluated at the $n = 11$ sub-leading-overlap peak ($h = 0.1223$), for varying disorder strength σ . (a) Loschmidt echo, averaged over 1000 disorder realizations for each σ . (b) Magnetization.

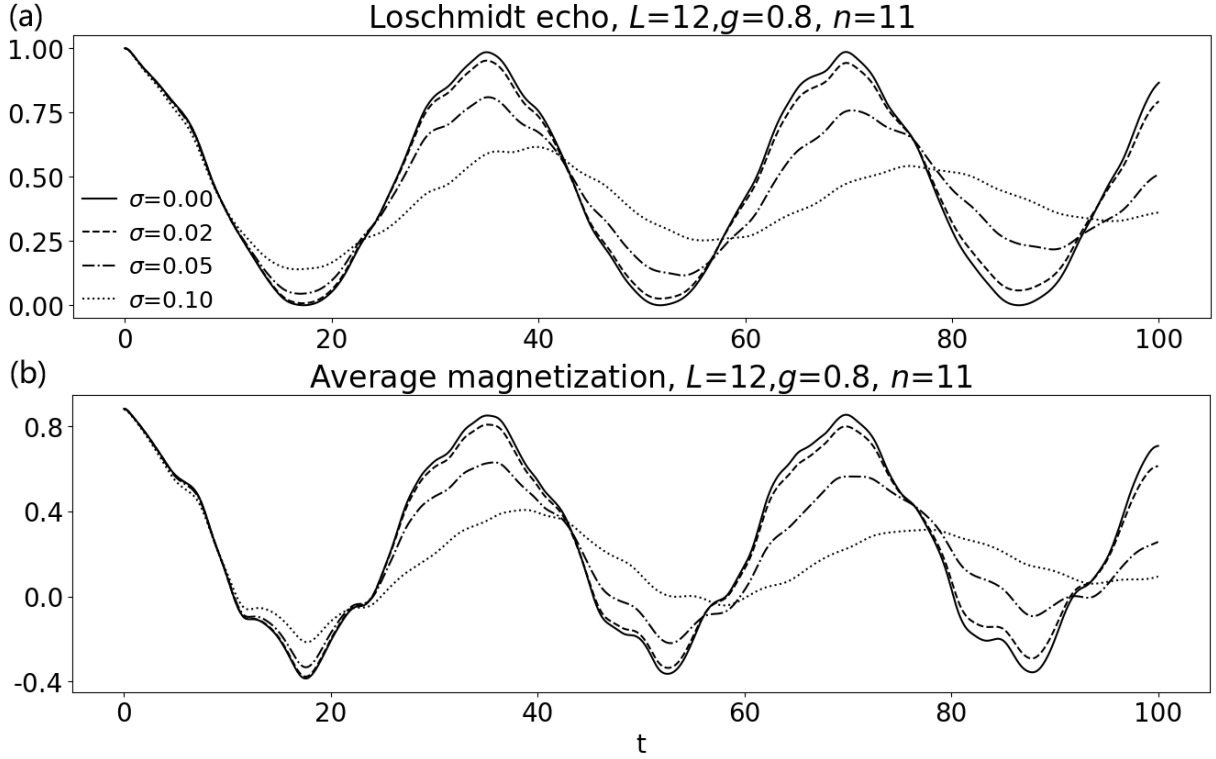


FIG. S2: Same as Fig. S1 but with transverse field increased to $g = 0.8$. At this value of g , the $n = 11$ resonance occurs at $h = 0.09875$.

IV. THE COHERENT DYNAMICS UNDER r^{-3} INTERACTION

Here we show that with the r^{-3} long-range Ising term included in the Hamiltonian, the coherent dynamics is again described by Eq. (4). In Fig. S3, for an $L = 12$ ring, we plot the dynamics at a parameter point, $g = 0.2$, $h = 0.965$, lying in the blue regime in the right panel of Fig. 4(a). During the oscillation, the magnetization shows a minimum at $\langle m \rangle = 0.5$, which fits well with the relation (7), $m(L, n) = \frac{L-2n}{L}$, when $n = 3$.

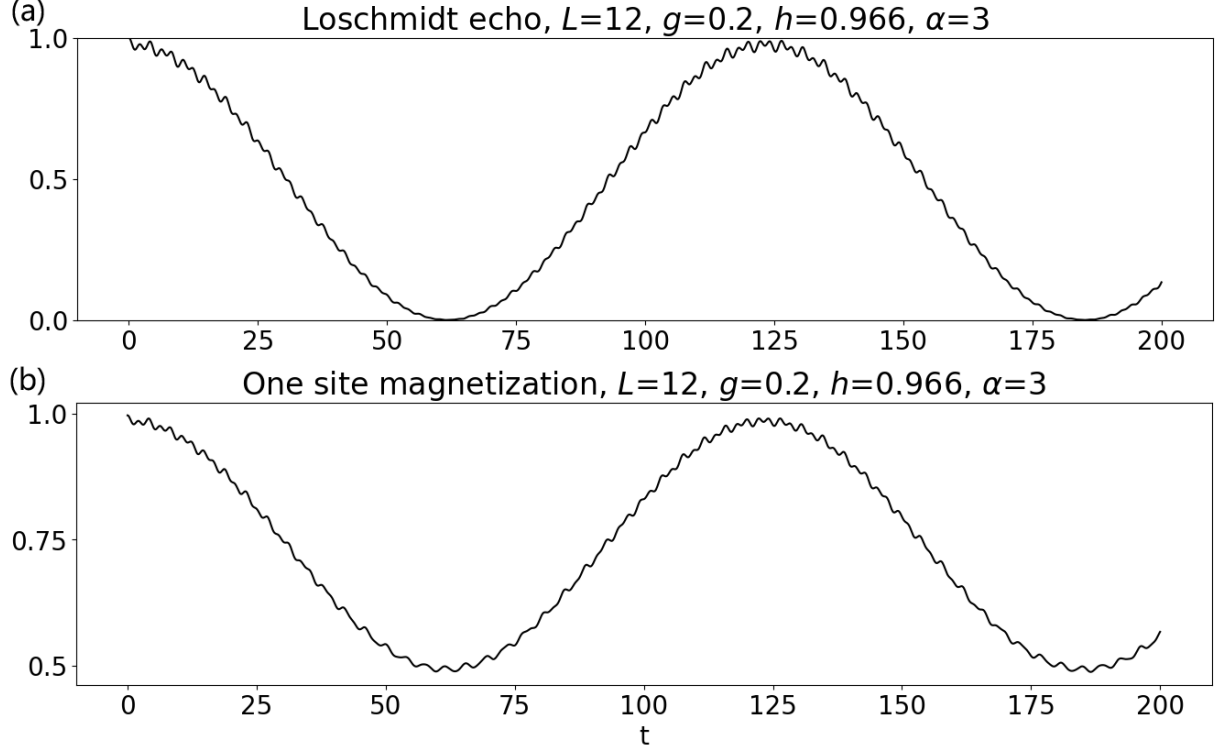


FIG. S3: The coherent dynamics of an $L = 12$ ring under r^{-3} interaction. (a) The return probability of the state with $g = 0.2$, $h = 0.966$ in r^{-3} interaction shows the two-state oscillation of the system. (b) The magnetization of the system.

V. ADDING A GLOBAL-RANGE SPIN-SQUEEZING INTERACTION

We off-resonantly couple the many-spin system to a cavity, with the following longitudinal qubit-oscillator interaction,

$$\begin{aligned} \hat{H} = & -J \sum_{i=1}^L \hat{\sigma}_i^z \hat{\sigma}_{i+1}^z - g \sum_{i=1}^L \hat{\sigma}_i^x + h \sum_{i=1}^L \hat{\sigma}_i^z \\ & + \omega_c \hat{a}^\dagger \hat{a} + g_c (\hat{a} + \hat{a}^\dagger) \left(\sum_{i=1}^L \hat{\sigma}_i^z \right). \end{aligned} \quad (16)$$

By adiabatically eliminating the cavity mode \hat{a} , we can engineer a global-range spin-squeezing term (with strength β) in the TLFIM Hamiltonian,

$$\begin{aligned} \hat{H} = & -J \sum_{i=1}^L \hat{\sigma}_i^z \hat{\sigma}_{i+1}^z - g \sum_{i=1}^L \hat{\sigma}_i^x + h \sum_{i=1}^L \hat{\sigma}_i^z \\ & - \frac{\beta J}{L} \left(\sum_{i=1}^L \hat{\sigma}_i^z \right)^2. \end{aligned} \quad (17)$$

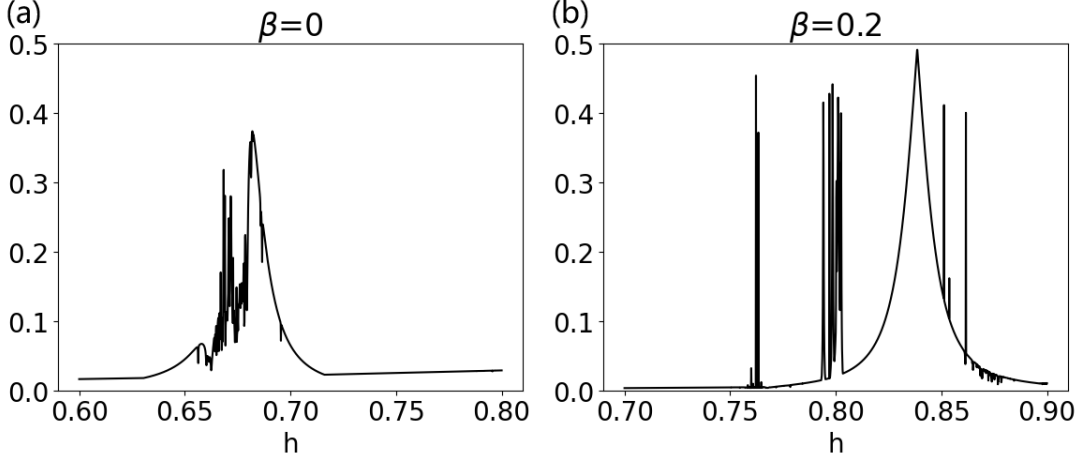


FIG. S4: The sub-leading overlap, P_{sub} , of state $|\Omega\rangle$ in an $L = 16$ ring around RBS order $n = 3$ with $g = 0.2$ and global-range interaction strength β . (a) $\beta = 0$, corresponding to the nearest-neighbour Ising model. (b) $\beta = 0.2$, the degeneracy between the single-bubble and multi-bubble manifolds is lifted.

This cavity-mediated interaction favours the ferromagnetism. When the chain length is large compared to the RBS order, such that $L > 4n$, a two-bubble state will exhibit a smaller magnetization strength compared to a single-bubble state, and thus a larger energy according to Eq. (17).

VI. COHERENT GENERATION OF MULTI-BUBBLE STATES FROM $|S_3\rangle$

Starting from the symmetric state $|S_3\rangle$ obtained in the main text, Eq. (3), we find that by modifying the field strengths h and g in Eq. (1), several coherent paths emerge that generate 2-state oscillations between $|S_3\rangle$ and various multi-bubble states. These paths are shown in Fig. S5(a), where we plot the sub-leading overlap P_{sub} between $|S_3\rangle$ and the eigenstates of \hat{H} in Eq. (1) for an $L = 8$ ring; the blue vertical line at $h = -2$ reflects the resonance between $|S_3\rangle$ and $|S_{101}\rangle = \frac{1}{\sqrt{L}} \sum_i \hat{S}_{i-1}^- \hat{S}_{i+1}^- |\Omega\rangle$, while the blue lines at $h = 1$ and $h = 2/3$ reveal the resonances $|S_3\rangle \leftrightarrow \frac{1}{\sqrt{2L}} \sum_i \hat{S}_{i-1}^- \hat{S}_i^- \hat{S}_{i+1}^- (\hat{S}_{i+3}^- \hat{S}_{i+4}^- + \hat{S}_{i-3}^- \hat{S}_{i-4}^-) |\Omega\rangle$ and $|S_3\rangle \leftrightarrow |\Omega\rangle$, respectively. Starting from these multi-bubble states, we could further identify coherent paths connecting to more exotic symmetric states. The states that are reversibly connected via these consecutive coherent 2-state oscillations form an orbital structure. The coherent preparation and interference of states within this orbital would be relevant to quantum information processing and interferometry-based precision measurements.

Moreover, as shown in Fig. S5(b), once the nearest-neighbour Ising term in Eq. (1) is replaced by the r^{-3} long-range interaction, the sub-leading overlap of $|S_3\rangle$ exhibits more exotic resonant features. The long-range part of the interaction not only shifts the resonant longitudinal field h , but also lifts the degeneracy of the multi-bubble manifold (see the splitting at $h \sim 2.1$), thereby enhancing the coherence. Furthermore, the interplay between the transverse field g and the long-range interaction induces a branch-splitting structure around $h \sim 2.1$. Such a non-analytic branch-splitting structure is expected to be non-perturbative and thus challenging to capture using perturbative approaches (such as SWT) starting from the unperturbed system at $g = 0$. The intriguing orbital structure associated with the long-range interaction will be examined in future work.

In Fig. S6, we plot the sub-leading overlap between the symmetric state $|S_3\rangle$ and the eigenstates of the TLFIM Hamiltonian for a chain of length $L = 12$. The same degeneracy lifting and branch-splitting behaviours are again revealed.

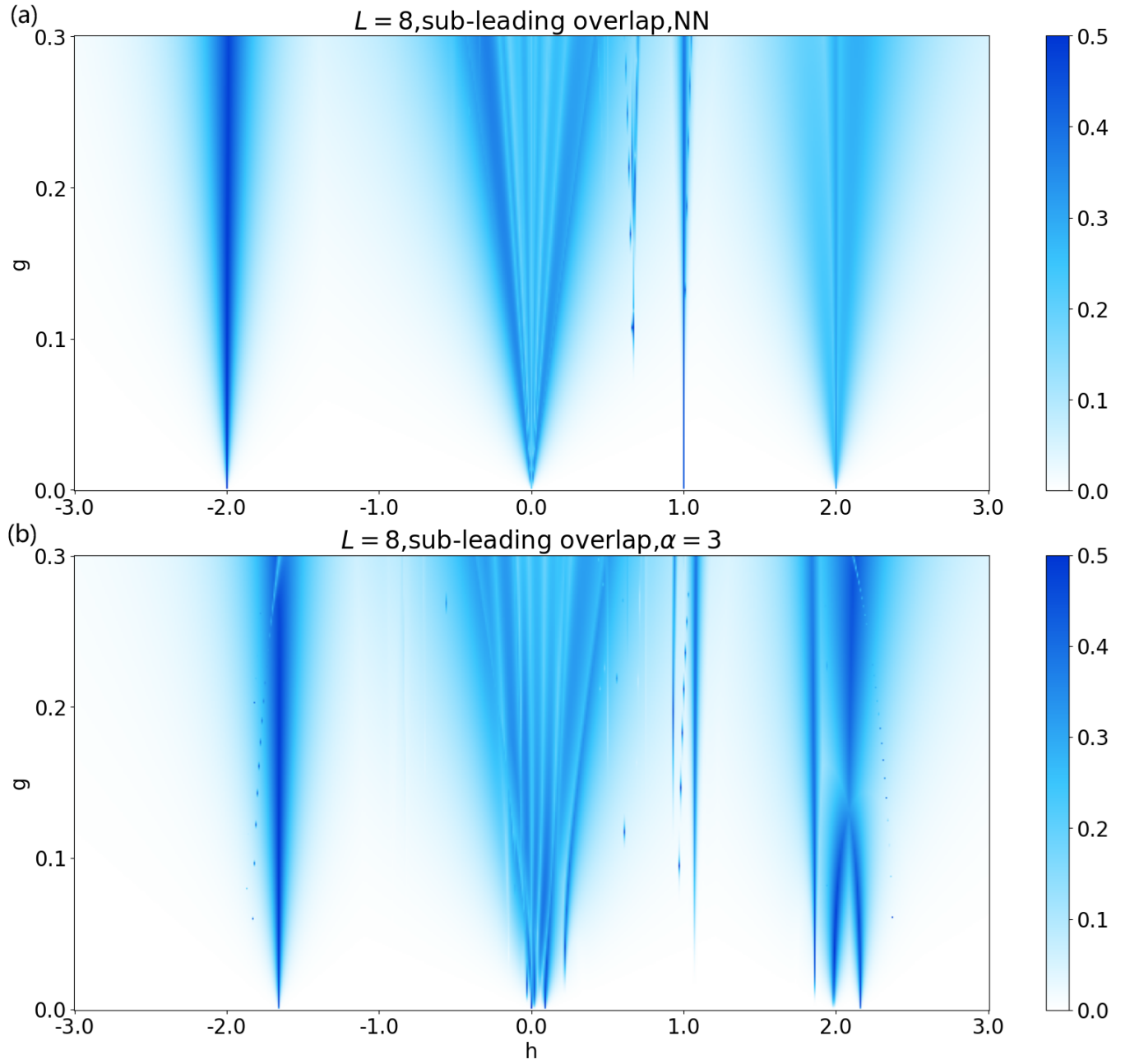


FIG. S5: The sub-leading overlap between $|S_3\rangle$ and the eigenstates of the Hamiltonian when $L = 8$. (a) The case for the NN Hamiltonian in Eq. (1). (b) The same as (a) but with the Ising term replaced by a long-range interaction $-J \sum_{i < j} |i - j|^{-3} \hat{\sigma}_i^z \hat{\sigma}_j^z$.

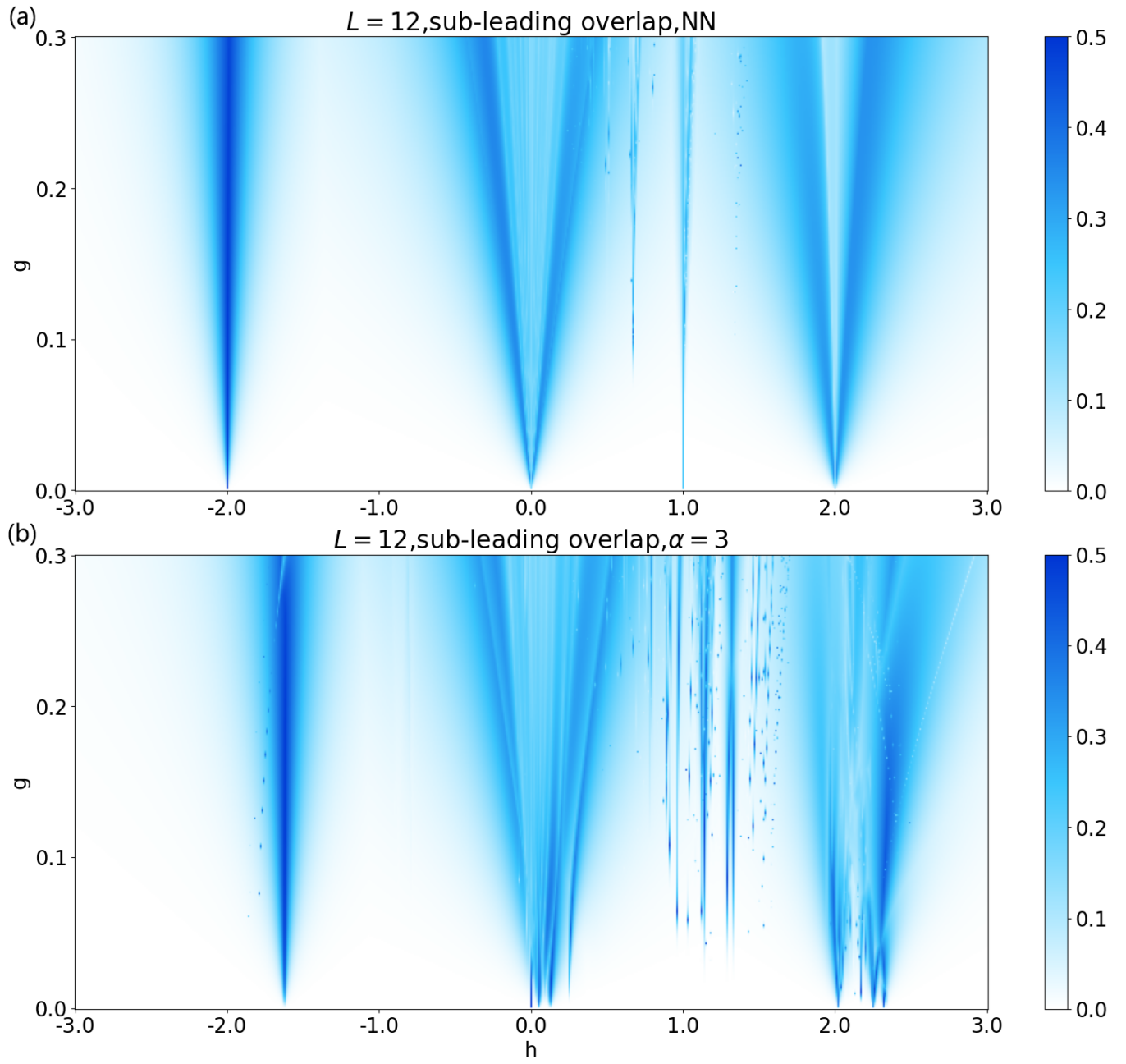


FIG. S6: The same as Fig. S5 but with $L = 12$.